

Neutron Bragg edge mapping of weld seams

Nikolay Kardjilov^a, Ingo Manke^a, André Hilger^b, Scott Williams^a, Markus Strobl^a, Robin Woracek^{a,c}, Mirko Boin^a, Eberhard Lehmann^d, Dayakar Penumadu^c, John Banhart^{a,b}

^aHelmholtz-Zentrum Berlin, Berlin, Germany

^bTechnical University Berlin, Berlin, Germany

^cUniversity of Tennessee, Knoxville, USA

^dPaul-Scherrer Institute, Villigen, Switzerland

Cold neutrons have a wavelength that is in the same range as the lattice spacings of most polycrystalline metallic materials. Imaging of such materials with monochromatic cold neutrons of different wavelengths provides a unique contrast due to coherent Bragg scattering. Additionally, the spectral positions of the Bragg edges can be mapped for each point of an image by using the transmission data of corresponding wavelength scans. We present investigations of welded components with such energy-selective neutron radiography around specific Bragg-edges in the transmission spectrum. Features in the local microstructure of the weld have been visualized.

Keywords: Neutron imaging, Bragg-edge mapping, Non-destructive testing

1. Introduction

Neutron imaging has a wide range of applications in materials science [1-10]. In recent years several new neutron imaging techniques have been introduced [1-3, 6, 11-18]. Some of them exploit the wavelength dependence of the transmission signal [19-26]. The neutron attenuation coefficient for polycrystalline materials decreases abruptly for certain neutron wavelengths – defining the so-called Bragg edges. The position of these edges is defined by crystal symmetry and the lattice parameters. At wavelengths greater than these critical values, no diffraction from given sets of $\{hkl\}$ planes can occur because the corresponding Bragg reflection angle reaches its maximum of $2\theta=180^\circ$ at the Bragg edge. Therefore, a sharp increase in transmission occurs.

Figure 1 illustrates the physical meaning of the Bragg edges in the attenuation spectrum of polycrystalline materials. For different wavelengths of the neutron spectrum a corresponding orientation of crystallites with defined d_{hkl} spacing can be found which fulfils Bragg's conditions:

$$2d_{hkl} \sin \theta = n\lambda \quad (1)$$

In Fig. 1 (left) different orientations of three crystallites are shown including the boundary condition of the Bragg edge at $\theta_{BE} = 90^\circ$. At this maximum orientation angle the neutrons with wavelength λ_{BE} undergo backscattering towards the source. For wavelengths longer than λ_{BE} no more Bragg scattering occurs because Bragg's condition can no longer be fulfilled and accordingly the transmitted neutron intensity increases. This gives rise to the observed dips in the attenuation spectrum as shown for polycrystalline iron in Fig. 1 (right) known as Bragg edges [3, 27, 28].

2. Bragg edge radiography of welds

Wavelength-dispersive transmission measurements (wavelength scan) can be performed by using of Time-of-Flight (TOF) technique at pulsed neutron sources (e.g. spallation sources) where the complete Bragg edge spectrum can be measured with the help of an energy resolving detector [25]. In case of steady state neutron sources (e.g. research reactors) the beam can be chopped by a chopper arrangement for a TOF measurement as described above or the transmission spectrum around Bragg edges for different materials can be measured by using a double crystal monochromator (pyrolytic graphite crystals with 0.8° mosaicity) in a combination with a standard imaging detector which has been demonstrated earlier at the cold neutron imaging instrument CONRAD at Helmholtz-Zentrum Berlin (HZB) [29, 30]. The wavelength resolution in the case of double crystal monochromatization is $\Delta\lambda/\lambda \sim 3\%$ with a field of view of $10 \text{ cm} \times 5 \text{ cm}$ (W x H).

A wavelength scan is obtained by collecting a radiographic image for a set of different wavelengths tuned by appropriate rotation and translation of the monochromators. Each image is normalised by dividing it by a corresponding reference image without the sample taken at the same wavelengths. Additional corrections for wavelength gradients are performed as described elsewhere [31].

Three corresponding images of welded austenitic steel plates [20] of 12 mm thickness were taken at different wavelengths using a high-resolution detector system with a pixel size of $13.5 \mu\text{m}$ [32] and are shown in Fig. 2.

The image contrast visible in the two images at wavelengths below the Bragg cut-off corresponding to the (110) lattice plane (at 3.8 and 4.0 Å) can be explained by diffraction contrast: in the dark areas of the corresponding two images, the Bragg-scattered neutrons are removed from the transmitted beam. Above the Bragg cut-off (at 4.2 Å) the Bragg's condition cannot be satisfied for any crystallite regardless its orientation and neutrons are no longer removed from the beam. Therefore, the contrast obtained is due to absorption only.

Image contrast can be caused both by local microstructure and local texture. Inside the weld the microstructure is different to the bulk material and not affected areas around it and it becomes therefore visible. The stripes can be assigned to a mixture of many elongated larger crystals which form during the welding process and have a preferred orientation. The margins of the weld, where heating of the material was limited are clearly visible. The stripes in the weld can be brighter or darker than the polycrystalline material around the weld. If the overall volume fraction of crystallites that scatter neutrons out of the direct line of sight is larger than in the surrounding polycrystalline matrix, the locations become darker. If it is smaller, they become brighter.

3. Bragg edge mapping

The position of the Bragg edges can be related to corresponding d_{hkl} spacings in case of a polycrystalline material without preferred crystal orientations and with a large number of crystallites [19, 25] (e.g. a powder sample). If areas of the sample undergo a phase transition where the crystal structure is influenced a shift of the Bragg edge positions will be recorded [25]. If the position of the Bragg cut-off is resolved with very high wavelength resolution ($\Delta\lambda/\lambda < 1\%$) then information about residual stresses can be obtained [26, 31].

In case of a small number of relative large crystallites such as inside the narrow weld seam, the Bragg edges are no longer sharply defined. The profile of the Bragg edge is correlated to the local microstructure, i.e. the orientations of the individual crystals or/and the mosaicity spread in case of a larger ensemble of crystallites. For single crystals the Bragg edge turns into a single dip where absorption is maximal due to the fulfilled Bragg condition (see Eq. 1). However, the recorded images are projections through the whole weld, i.e. at each point, a sufficient number of crystallites can be found to define and fit a Bragg edge. In this case, the Bragg cut-off is defined by the crystallite(s) that fulfil(s) the Bragg edge condition Eq. 1 at the highest possible wavelength. The number of crystallites for the weld shown in Fig. 2 can be

estimated to be a few dozen through the weld thickness taking into account that the lateral size of the grains is in the order of a millimetre (confirmed by EBSD measurement on the weld surface [33]) and the thickness of the weld is 12 mm.

By recording radiographs at different (equidistant) wavelengths, one obtains the full information of attenuation for each point of the sample. As a Bragg edge originates in the diffraction from specific crystal lattice planes of a material, lattice changes due to changes in the crystal structure can be imaged with this method by mapping the position of a Bragg edge. This method was applied to the images recorded of a weld seam (see Fig. 2). The radiographs were taken at wavelengths from 2.2 Å to 6.4 Å in steps of 0.1 Å. In this way the attenuation curve for each point of the sample can be recorded as a function of the neutron wavelength where a fitting model can be used to determine the Bragg edge positions as shown elsewhere [26]. In our case a simplified procedure was used where the attenuation curve for each pixel was derived and the resulted curve was fitted by a Gauss function (see Fig. 3). The centre of the Gaussian is presumably taken to be the edge position.

The positions of the Bragg edges in the map presented vary from 3.8 Å to 4.1 Å, which corresponds to up to 7 % shift of position. This shift cannot be explained by residual stresses which are in the range of 0.1% only. Such large shifts can only be explained by a change in the Bragg edge profile due to the limited amount of crystallites at the specific locations, because larger crystallites have been formed there and no homogenous orientation distribution of the crystallites is to be expected in this case.

In any case the areas associated with different Bragg edges shown on the map in Fig. 4 have different microstructures which can be a reason for enhanced crack propagation at the crystal boundaries. Therefore such kind of investigations provides qualitative information for probable safety issues in weld seams.

4. Conclusions

Imaging with monochromatic neutrons provides a unique contrast originating from coherent Bragg scattering in polycrystalline materials. The advantage of using neutrons is their high penetration depth and suitable wavelength interval which matches the range of d_{hkl} spaces in polycrystalline metallic materials. Radiographic investigations around the Bragg edge of a material can be used to determine the position of the Bragg edge in two dimensions. This enables visualization of changes in local microstructures and textures and can help to map variations of chemical compositions or phase composition. The potential of Bragg edge imaging for providing a contrast that is complementary to the classical absorption techniques is clearly visible.

References

- [1] M. Strobl, I. Manke, N. Kardjilov, A. Hilger, M. Dawson, J. Banhart, *Journal of Physics D-Applied Physics*, 42 (2009).
- [2] N. Kardjilov, I. Manke, A. Hilger, M. Strobl, J. Banhart, *Materials Today* 14 (2011) 248-256.
- [3] J. Banhart, *Advanced Tomographic Methods in Materials Research and Engineering*, in, Oxford University Press, Oxford, UK, 2008.
- [4] R.J. Bellows, M.Y. Lin, M. Arif, A.K. Thompson, D. Jacobson, *Journal of The Electrochemical Society*, 146 (1999) 1099-1103.
- [5] B. Schillinger, E. Lehmann, P. Vontobel, *Physica B: Condensed Matter*, 276-278 (2000) 59-62.
- [6] P. Vontobel, E.H. Lehmann, R. Hassanein, G. Frei, *Physica B: Condensed Matter*, 385-386 (2006) 475-480.
- [7] A. Schröder, K. Wippermann, W. Lehnert, D. Stolten, T. Sanders, T. Baumhöfer, N. Kardjilov, A. Hilger, J. Banhart, I. Manke, *Journal of Power Sources*, 195 (2010) 4765-4771.

- [8] I. Manke, M. Strobl, N. Kardjilov, A. Hilger, W. Treimer, M. Dawson, J. Banhart, *Nuclear Instruments and Methods in Physics Research Section A: Accelerators, Spectrometers, Detectors and Associated Equipment*, 610 (2009) 622-626.
- [9] D. Goers, M. Holzapfel, W. Scheifele, E. Lehmann, P. Vontobel, P. Novák, *Journal of Power Sources*, 130 (2004) 221-226.
- [10] M. Michaloudaki, E. Lehmann, D. Kosteas, *International Journal of Adhesion and Adhesives*, 25 (2005) 257-267.
- [11] N. Kardjilov, I. Manke, M. Strobl, A. Hilger, W. Treimer, M. Meissner, T. Krist, J. Banhart, *Nature Physics*, 4 (2008) 399-403.
- [12] M. Strobl, C. Grünzweig, A. Hilger, I. Manke, N. Kardjilov, C. David, F. Pfeiffer, *Physical Review Letters*, 101 (2008) 123902.
- [13] I. Manke, N. Kardjilov, R. Schäfer, A. Hilger, M. Strobl, M. Dawson, C. Grünzweig, G. Behr, M. Hentschel, C. David, A. Kupsch, A. Lange, J. Banhart, *Nature Communications*, 1 (2010) 125, DOI: 110.1038/ncomms1125.
- [14] C. Grünzweig, C. David, O. Bunk, M. Dierolf, G. Frei, G. Kühne, J. Kohlbrecher, R. Schäfer, P. Lejcek, H.M.R. Rønnow, F. Pfeiffer, *Physical Review Letters*, 101 (2008) 025504.
- [15] M. Strobl, W. Treimer, P. Walter, S. Keil, I. Manke, *Applied Physics Letters*, 91 (2007) 254104.
- [16] M. Strobl, A. Hilger, N. Kardjilov, O. Ebrahimi, S. Keil, I. Manke, *Nuclear Instruments and Methods in Physics Research Section A: Accelerators, Spectrometers, Detectors and Associated Equipment*, 605 (2009) 9-12.
- [17] M. Strobl, C. Pappas, A. Hilger, S. Wellert, N. Kardjilov, S.O. Seidel, I. Manke, *Physica B: Condensed Matter*, 406 (2011) 2415-2418.
- [18] M. Dawson, I. Manke, N. Kardjilov, A. Hilger, M. Strobl, J. Banhart, *New Journal of Physics*, 11 (2009).

- [19] W. Kockelmann, G. Frei, E.H. Lehmann, P. Vontobel, J.R. Santisteban, Nucl Instrum Meth A, 578 (2007) 421-434.
- [20] E.H. Lehmann, G. Frei, P. Vontobel, L. Josic, N. Kardjilov, A. Hilger, W. Kockelmann, A. Steuer, Nuclear Instruments and Methods in Physics Research Section A: Accelerators, Spectrometers, Detectors and Associated Equipment, 603 (2009) 429-438.
- [21] L. Josic, E.H. Lehmann, A. Kaestner, Nuclear Instruments and Methods in Physics Research A, doi:10.1016/j.nima.2010.12.120 (2010).
- [22] E.H. Lehmann, L. Josic, G. Frei, Neutron News, 20 (2009) 20-23.
- [23] L. Josic, A. Steuer, E. Lehmann, Applied Physics A, 99 (2010) 515-522.
- [24] W. Treimer, M. Strobl, N. Kardjilov, A. Hilger, I. Manke, Applied Physics Letters, 89 (2006).
- [25] J.R. Santisteban, L. Edwards, M.E. Fitzpatrick, A. Steuer, P.J. Withers, Appl Phys Mater, 74 (2002) S1433-S1436.
- [26] J.R. Santisteban, L. Edwards, M.E. Fitzpatrick, A. Steuer, P.J. Withers, M.R. Daymond, M.W. Johnson, N. Rhodes, E.M. Schooneveld, Nucl Instrum Meth A, 481 (2002) 765-768.
- [27] K. Meggers, H.G. Priesmeyer, M. Stalder, S. Vogel, W. Trela, Physica B, 234 (1997) 1160-1162.
- [28] H.G. Priesmeyer, M. Stalder, S. Vogel, K. Meggers, W. Trela, Neutrons in Research and Industry, International Conference, 2867 (1997) 164-167
638.
- [29] N. Kardjilov, A. Hilger, I. Manke, M. Strobl, M. Dawson, J. Banhart, Nucl Instrum Meth A, 605 (2009) 13-15.

- [30] N. Kardjilov, A. Hilger, I. Manke, M. Strobl, M. Dawson, S. Williams, J. Banhart, Nuclear Instruments and Methods in Physics Research Section A: Accelerators, Spectrometers, Detectors and Associated Equipment, 10.1016/j.nima.2011.01.067 (2011).
- [31] R. Woracek, D. Penumadu, N. Kardjilov, A. Hilger, M. Strobl, R.C. Wimpory, I. Manke, J. Banhart, J Appl Phys, 109 (2011).
- [32] E.H. Lehmann, G. Frei, G. Kuhne, P. Boillat, Nucl Instrum Meth A, 576 (2007) 389-396.
- [33] private communication with E. H. Lehmann and L. Josic (Paul-Scherrer Institute, Switzerland)

Correspondence address:

Dr. Nikolay Kardjilov

Helmholtz-Zentrum Berlin, Hahn-Meitner Platz 1, 14109 Berlin, Germany

Tel.: +49 30 80 62 42298

Fax: +49 30 80 62 43059

e-mail: kardjilov@helmholtz-berlin.de

List of figure and table captions.

Figure 1: Bragg diffraction in polycrystalline material represented schematically (left). An example of the energy dependent attenuation spectrum for iron is given on the right. The wavelengths at which Bragg's law is satisfied in the sketch on the left are given by color map. The condition $\theta_{BE} = 90^\circ$ corresponds to a discontinuity of the attenuation coefficient.

Figure 2: Wavelength dispersive neutron images of weld joint between two austenitic steel plates taken with high spatial resolution. a) Photographic image. b) Radiographic images at three wavelengths around the Bragg edge for iron corresponding to (110) lattice space (as shown above). Pixel size 27 μm , exposure time 300 s, 50- μm thick $^6\text{LiZnS}$ scintillator.

Figure 3: The first derivative of the attenuation spectrum around the Bragg edge. The parameters of the Gaussian fit provide information about the position of the Bragg edge (x_c). From the fit parameters the position of the Bragg edge was determined. The positions were converted into grey values and form a map as given in Fig. 4.

Figure 4: Map of the position of the Bragg edge for a weld seam between two plates of austenitic steel.

Figures.

Figure 1:

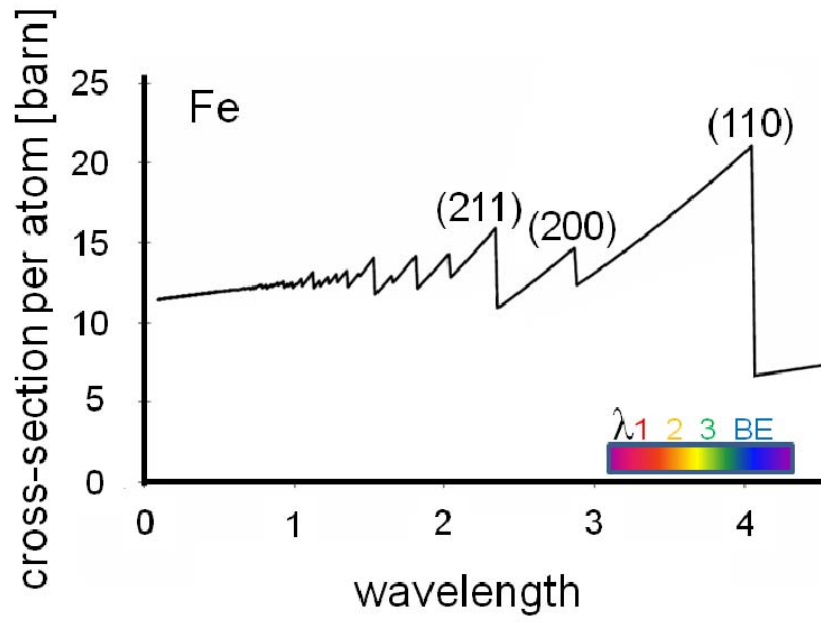
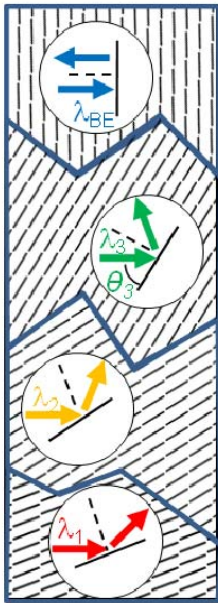


Figure 2:

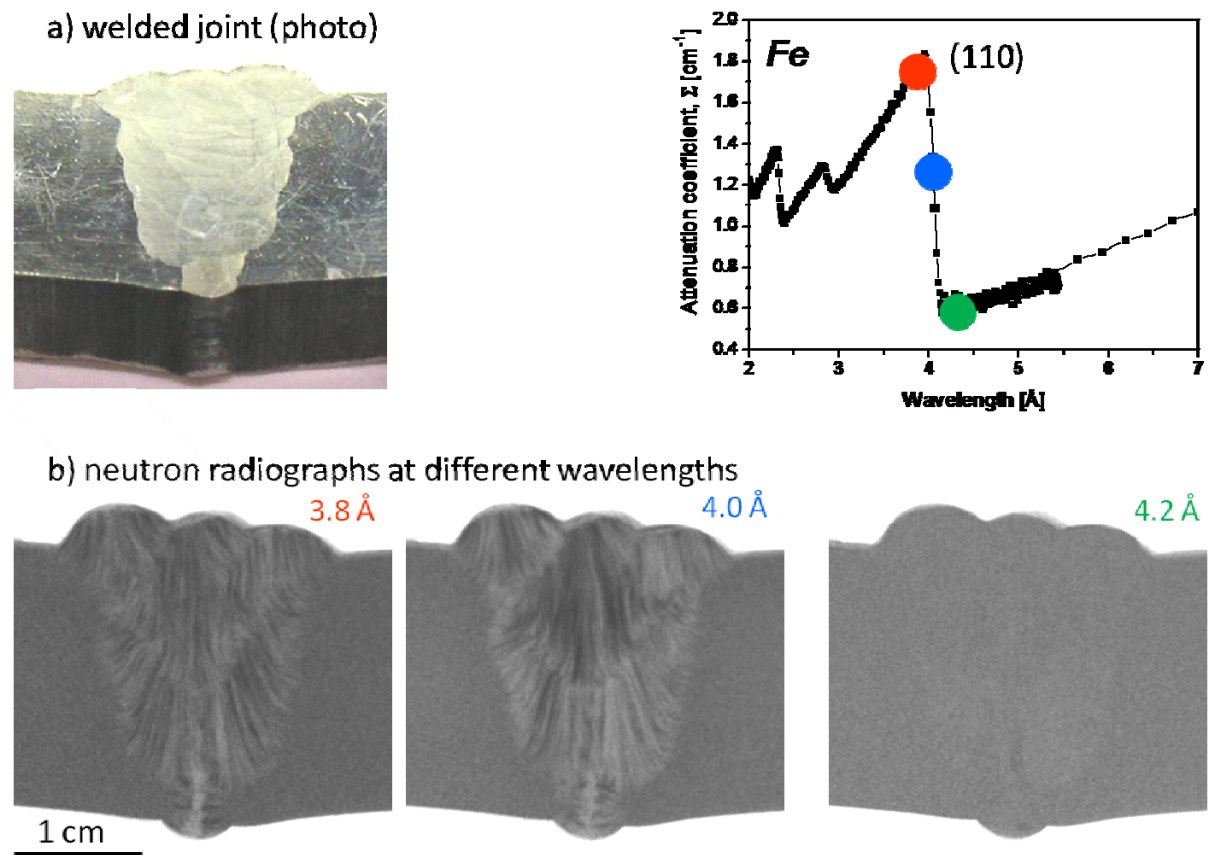


Figure 3:

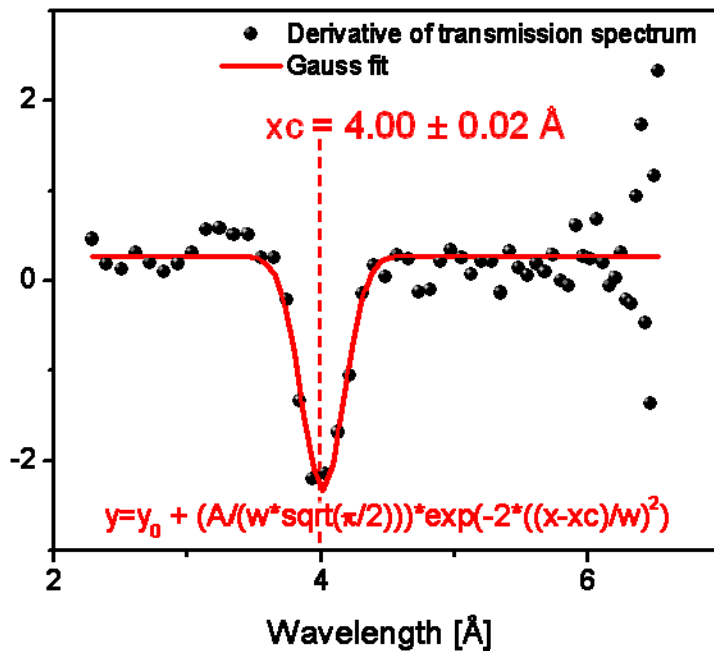


Figure 4:

